

# Supplemental Information

# General Information

# Why is specular neutron reflectometry so special?

<> Neutron reflectometry (NR) is a valuable probe of the structure of both hard and soft condensed matter in thin film or multilayered form -- particularly for hydrogenous and magnetic materials. NR can see *beneath* the surface and provide quantitative structural information from *everywhere within* the film on a nanometer scale.

<> Both “forward” and “inverse” scattering problems for specular neutron reflection are mathematically solvable, exactly, from first-principles quantum theory. The mathematically unique solutions are thus far only possible in one dimension and for non-absorbing potentials of finite extent.

<> Phase-sensitive neutron specular reflectometry, employing references, enables direct inversion of composite reflectivity data sets to yield a unique scattering length density depth profile for an “unknown” film of interest, without fitting or any adjustable parameters.

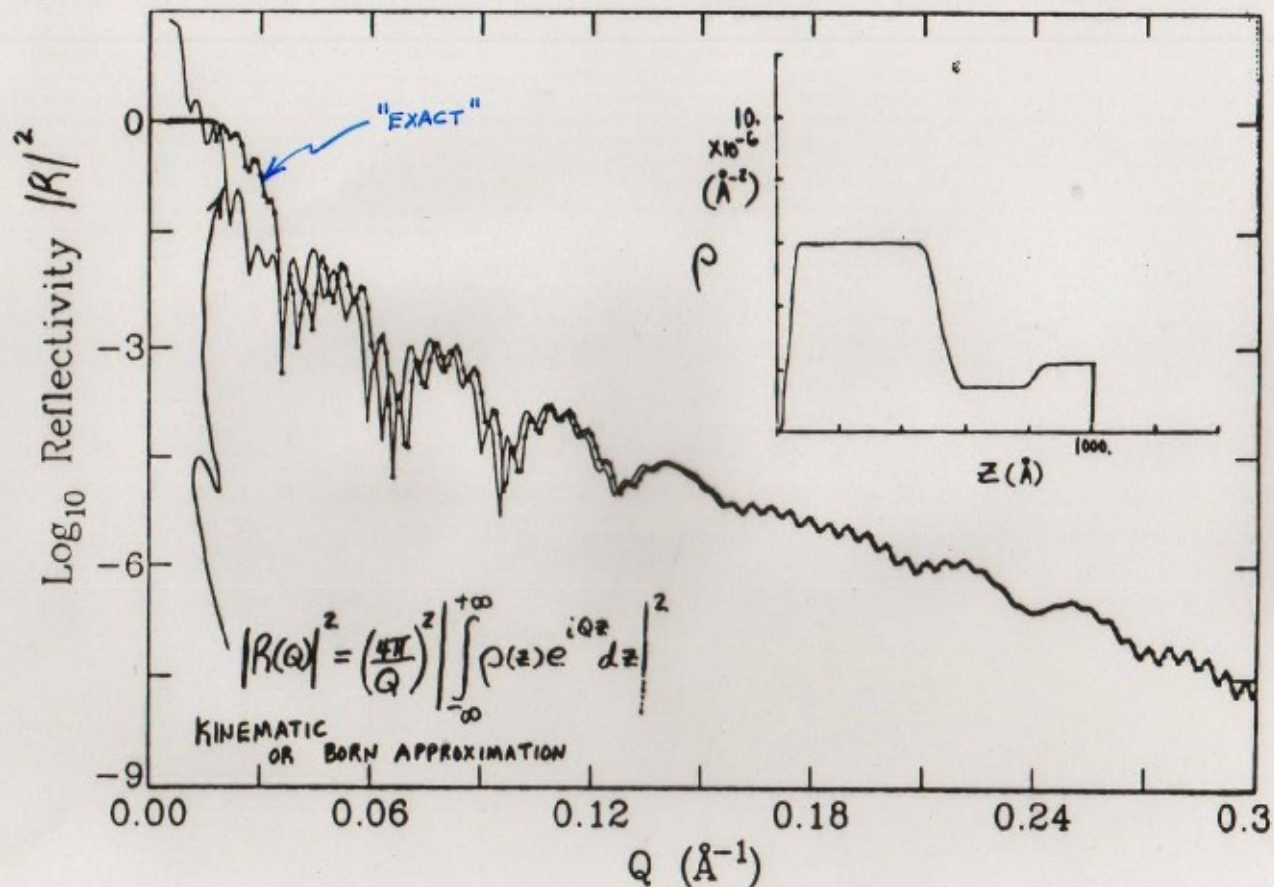
<> The spatial resolution and accuracy of the SLD profile thereby obtained is limited only by the statistical uncertainty in the measured reflected intensities and truncation of the reflectivity data sets at the maximum value of wavevector transfer attainable.

# Importance of Sample System Preparation

- > The great success in using neutron reflection/diffraction to study thin film systems of hard condensed matter, in particular the structures and fundamental interactions in magnetic materials, is largely due to the ability to tailor, with atomic-layer accuracy and precision, single-crystalline, layered sandwiches and superlattices (using vapor deposition techniques such as molecular beam epitaxy in ultra-high vacuum). Advances in film deposition techniques and lithography continue at a remarkable rate.
- > Similarly, neutron reflectometry in principle can be applied as a probe to further our understanding of the structure and function of molecules in lipid membranes, of relevance in biology and bioengineering, when comparable control over the fabrication of model systems is achieved. Great progress has been made toward realizing this goal in practice. However, we are still at a relatively early stage of development in our ability to engineer soft condensed matter films on atomic and nanometer scales. Progress can be expected as efforts in creating and manipulating membrane / molecular systems accelerates.
- > Employing phase-sensitive methods in reflectivity measurements ensures a unique scattering length density (SLD) depth profile. Additional application of hydrogen / deuterium substitution techniques and comparison with molecular dynamics calculations assures a correspondingly high degree of certainty of obtaining an unambiguous chemical composition depth profile.

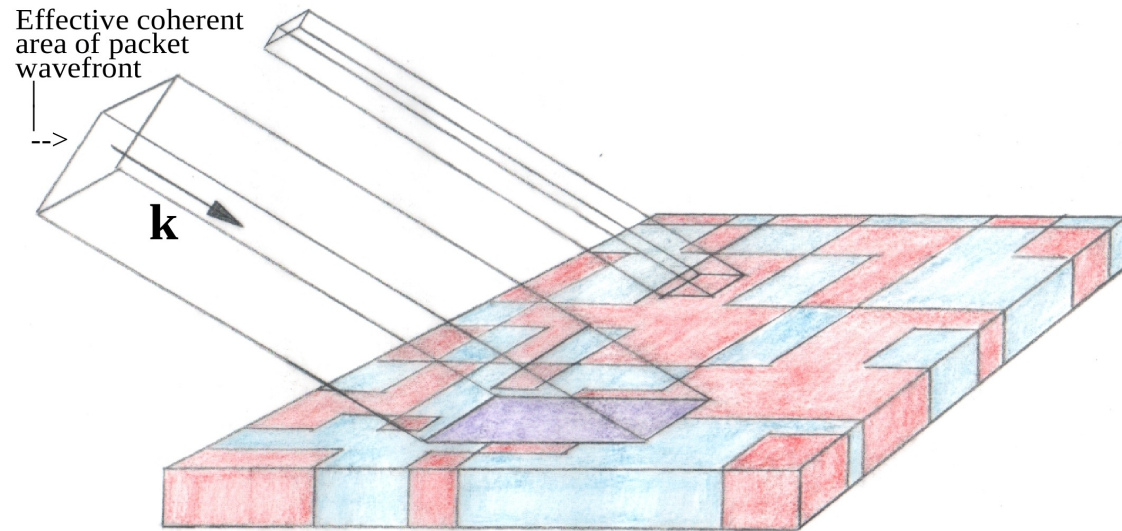


**PROBLEM:** BORN APPROXIMATION FAILS AT SUFFICIENTLY SMALL Q — MUST THEN USE EXACT THEORY



Comparison between kinematic (line) and dynamic (triangle + line) plus-state reflectivities for a density profile similar to that of Fig.2 as described in the text.

Because the Born approximation often fails to be of sufficient accuracy for specular reflection at at low  $Q$ , an exact solution of the one-dimensional Schroedinger wave equation of motion becomes necessary. A practical method of solving this equation is possible, by imposing certain boundary conditions in piece-wise continuous fashion.



The effective transverse coherence area perpendicular to the propagation direction of the neutron wave packet is projected onto the film surface defining an area over which in-plane variations in SLD are averaged over in the specular process (note that the glancing angle of incidence enhances the projection along one in-plane direction):

$$r = (4\pi / (iQ)) \int_{-\infty}^{+\infty} \psi_{kz}(z) \langle \rho(x,y,z) \rangle_{x,y} e^{ikz} dz$$

$$\langle \rho(x,y,z) \rangle_{x,y} = (1/A) \int_{-\infty}^{+\infty} \rho(x,y,z) dx dy$$

The length scale of the SLD variations must be small enough for effective averaging to occur within the projected area. (The purple shaded area is meant to represent the coherent average of separate areas of “red” and “blue” SLD.) If not, then the net measured reflected intensity  $|r|^2$  is an area-weighted sum of reflectivities, each corresponding to an in-plane averaged SLD within a particular respective area, as depicted schematically in the figure above for the case of two distinct areas of different SLD (red and blue areas):

$$|r_{\text{NET MEASURED}}|^2 = (A_{\text{RED}} / A_{\text{TOTAL}}) |r_{\text{RED}}|^2 + (A_{\text{BLUE}} / A_{\text{TOTAL}}) |r_{\text{BLUE}}|^2$$

# Soft Condensed Matter Membrane Systems



# Neutron reflectometry studies of membrane-bound tubulin reveal an amphipathic helical binding motif

D. P. Hoogerheide,<sup>1</sup> S. Yu. Noskov,<sup>2</sup> D. Jacobs,<sup>3</sup> L. Bergdoll,<sup>4</sup> V. Silin,<sup>5</sup> D. Worcester,<sup>1</sup> J. Abramson,<sup>4,6</sup> H. Nanda,<sup>1,7</sup> T. K. Rostovtseva,<sup>3</sup> and S. M. Bezrukov<sup>3</sup>

Bilayer lipid membranes (BLMs) form barriers that separate the interior from the exterior of the cell and divide the cell into specialized compartments called organelles. Proteins that are embedded into BLMs, known as membrane proteins, play diverse roles, including the transportation of various ions, metabolites, proteins, DNA, etc., across the BLMs, thus providing communication pathways between cells and between organelles inside cells. This function is so crucial for health and disease that while membrane proteins account for about 20 % of known proteins [1], they comprise 70 % of known drug targets [2]. In humans, mitochondria are the organelles responsible for energy conversion, with two main purposes: to store energy, and to produce heat that maintains body temperature. However, mitochondria themselves are also the sources of the reactive oxygen species that damage mitochondria, mitochondrial DNA, and other cellular components. Therefore, maintaining the appropriate conditions that provide sufficient energy for cellular functions and limit the production of chemically damaging reactive oxygen species is crucial for cell life and death. Recent evidence indicates that the regulation of this equilibrium is accomplished at least in part by a complex of the mitochondrial voltage-dependent anion channel (VDAC), a passive transport channel of the mitochondrial outer membrane (MOM), and dimeric tubulin [3], which is best known as a structural protein in microtubules. The association of tubulin with the MOM is particularly suggestive given the role of microtubule-targeting drugs (MTDs) in chemotherapy [4]. In this work we shed light on the role of dimeric tubulin in regulating mitochondrial bioenergetics by investigating the binding of tubulin to biomimetic mitochondrial membranes using a combination of neutron reflectometry (NR) and molecular dynamics (MD) simulations [5].

Tubulin is a heterodimer comprising  $\alpha$  and  $\beta$  subunits, which have similar spatial arrangements but different amino acid sequences. In microtubules, the exposed end is always the  $\beta$  subunit; as a result, all MTDs bind to the  $\beta$  subunit [4]. Remarkably, in an *in vitro* system the rate of interaction between tubulin and a single VDAC channel was observed to depend strongly on the lipid composition of the BLM in which VDAC was embedded. In particular, the interaction rate increased by two orders of magnitude if a lamellar (i.e. preferring a flat membrane geometry) dioleoylphosphatidylcholine

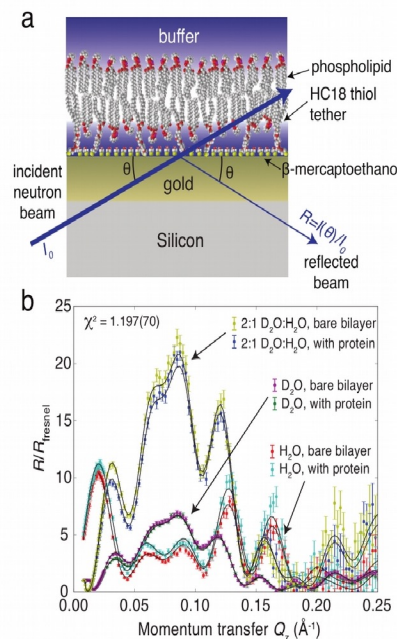


**FIGURE 1:** Neutron reflectometry (NR) experiment with a sparsely tethered lipid bilayer membrane (stBLM). (a) Schematic of the stBLM and scattering geometry. Sparse tethering is achieved by using  $\beta$ -mercaptoethanol as a spacer molecule. (b) NR data, showing the differences between the three deuteration levels of the buffer solutions. Data are normalized to the Fresnel reflectivity expected from a silicon/buffer interface. Solid lines show the fit to a theoretical model of the bilayer with bound tubulin.

(DOPC) membrane was replaced with the non-lamellar (preferring a curved membrane geometry) dioleoylphosphatidylethanolamine (DOPE) [6], suggesting that tubulin is able to distinguish between these two lipid species. Furthermore, these results indicate that the first step of the VDAC-tubulin interaction involves tubulin binding to the lipid membrane surface.

In this study, we determined the orientation of membrane-bound tubulin—and hence the face of the tubulin molecule that is in contact with the membrane surface—by NR on sparsely tethered BLMs (stBLMs). NR reports on the depth profile of the interfacial components, including the stBLM and any membrane-bound tubulin (Figure 1a). Thus, NR is well suited to determine the spatial extent of the protein in and away from the BLM and yields a potential family of binding surfaces to be investigated by computational methods and amino acid sequence analysis.

For these experiments, an stBLM was composed of a 1:1 molar ratio of DOPC:DOPE. This lipid composition closely mimics the mitochondrial outer membrane, in which the ratio of PC to PE headgroups is about 3:2. The stBLM was bathed in an aqueous 1 mol/L KCl solution buffered at pH 7.4 by 5 mM HEPES. The reflectivity of the stBLM was measured using 4.75  $\text{\AA}$  neutrons on the NCNR NG7 horizontal reflectometer. To provide contrast between the various components of the stBLM system, a sequence of reflectometry measurements was performed using buffers in 100 %  $D_2O$ , 100 %  $H_2O$ , and a 2:1  $D_2O:H_2O$  mixture. This procedure was then repeated in the presence of 600 nM tubulin dimers (a physiologically relevant concentration).

The reflectivity data (Figure 1b) were then fit to an stBLM model (Figure 2a). Because it accounts for known molecular volumes, molecular connectivity, and stoichiometric constraints, the model is highly constrained. To determine the orientation of the tubulin dimer on the lipid substrate, the expected scattering profile was calculated for various Euler rotations of the known X-ray crystal structure of tubulin. Due to the elongated geometry of the tubulin dimer, the NR profile is very sensitive to the tilt angle  $\beta$  (Figure 2b), allowing a precise determination of this tilt angle,  $\approx 60^\circ$ , from the optimization of the experimental NR data to the stBLM/tubulin model.

To complement the NR results, molecular dynamics simulations were performed to confirm the orientation of  $\alpha$ -tubulin on a DOPE membrane. A range of possible orientations were evaluated using a coarse-grained model of the protein; likely orientations were then optimized using atomistic simulations. The tilt angle of the tubulin on the membrane surface is consistent with that observed by NR, while the atomistic nature of the simulations allows us to identify the particular domain of the tubulin protein that is responsible for binding to the membrane surface. A comparison of the MD and NR results is shown in Figure 2b.

The binding sequence is shown in green in Figure 2b. Notably, it is on the  $\alpha$ -tubulin subunit, rather than on the  $\beta$ -tubulin subunit which is conventionally targeted by chemotherapeutics. When associated with the membrane, this amino acid sequence likely adopts an  $\alpha$ -helical structure which has opposing hydrophobic and hydrophilic faces, i.e. an amphipathic helix. Such helices are oriented at the interface between the polar lipid headgroups and the hydrophobic lipid tails. We have also shown [5] that the affinity of this helix to the mixed PC/PE membranes considered here depends strongly on the amount of PE lipid. This suggests that the lipid composition of the mitochondrial outer membrane could regulate tubulin binding, which in turn modulates VDAC permeability and consequently mitochondrial function. We hypothesize that this selectivity for the uncharged PE lipids may have developed to overcome electrostatic

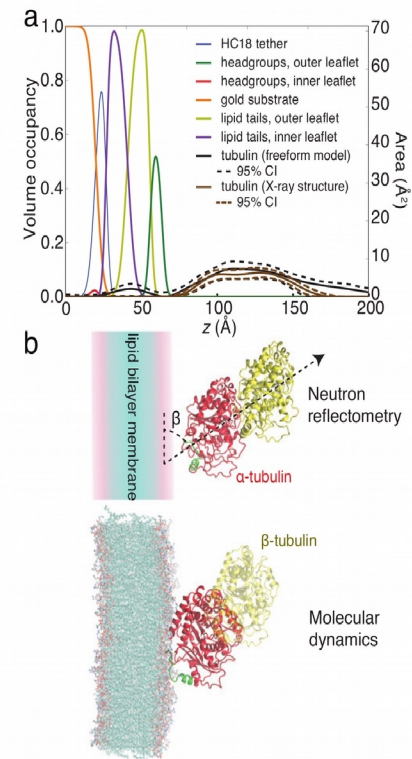


**FIGURE 2:** Results of modeling the tubulin-stBLM system. (a) Volume occupancy representation showing the position of various chemical species. (b) Visual representation of the structure of membrane-bound tubulin as determined by NR (top) and atomistic molecular dynamics simulations of the  $\alpha$ -tubulin subunit (bottom). The Euler angle  $\beta$  is  $\approx 60^\circ$ . The  $\alpha$ -tubulin subunit is shown in red; the  $\beta$ -tubulin subunit in yellow; and the binding site in green.

repulsion between the negatively charged components of the mitochondrial outer membrane and the tubulin molecule.

## References

- M. S. Almen, K. J. Nordstrom, R. Fredriksson, and H. B. Schioth, *BMC Biology* **7**, 50 (2009).
- M. A. Yildirim, K.-I. Goh, M. E. Cusick, A.-L. Barabasi, and M. Vidal, *Nat. Biotechnol.* **25**, 1119 (2007).
- T. K. Rostovtseva, K. L. Sheldon, E. Hassanzadeh, C. Monge, V. Saks, S. M. Bezrukov, and D. L. Sackett, *Proc. Natl. Acad. Sci.* **105**, 18746 (2008).
- J. J. Field, A. B. Waight, and P. D. Senter, *Proc. Natl. Acad. Sci.* **111**, 13684 (2014).
- D. P. Hoogerheide, S. Y. Noskov, D. Jacobs, L. Bergdoll, V. Silin, D. Worcester, J. Abramson, H. Nanda, T. K. Rostovtseva, and S. M. Bezrukov, *Nat. Struct. Mol. Biol.*, submitted (2016).
- T. K. Rostovtseva, P. A. Gurney, M. Y. Chen, and S. M. Bezrukov, *J. Biol. Chem.* **287**, 29589 (2012).

<sup>1</sup> NIST Center for Neutron Research, National Institute of Standards and Technology, Gaithersburg, MD 20899

<sup>2</sup> University of Calgary, Calgary, AB, Canada, T2N 1N4

<sup>3</sup> Eunice Kennedy Shriver National Institute of Child Health and Human Development, National Institutes of Health, Bethesda, MD 20892

<sup>4</sup> University of California Los Angeles, Los Angeles, CA 90095

<sup>5</sup> University of Maryland, Rockville, MD 20850

<sup>6</sup> Institute for Stem Cell Biology and Regenerative Medicine, National Centre for Biological Sciences-Tata Institute of Fundamental Research, Bellary Road, Bangalore-560065, Karnataka, India

<sup>7</sup> Carnegie Mellon University, Pittsburgh, PA 15213

# Layered Magnetic Film Systems and Polarized Neutron Reflectometry



# Realization of ground-state artificial skyrmion lattices at room temperature

D. A. Gilbert,<sup>1,2</sup> B. B. Maranville,<sup>2</sup> A. L. Balk,<sup>3,4</sup> B. J. Kirby,<sup>2</sup> P. Fischer,<sup>5,6</sup> D. T. Pierce,<sup>3</sup> J. Unguris,<sup>3</sup> J. A. Borchers,<sup>2</sup> and K. Liu<sup>1</sup>

Moore's Law has been the icon of the computer revolution for nearly 50 years, but recent challenges with heat management and miniaturization have signaled its impending end. Spintronics – data and logic technologies that use the electron spin, in addition to the electron charge – offer a new approach to ultra-low power information technologies that may reinvigorate Moore's Law. One promising spintronic technology is the magnetic skyrmion. Skyrmions are specialized configurations of magnetic moments into topologically-protected structures; a typical skyrmion structure, shown in Fig. 1, possesses a core and perimeter with opposite out-of-plane spin orientations, and a closed, continuous in-plane winding of magnetic moments between. These structures can be realized on the atomic scale, moved with very low electrical current densities, and are robust against moderate perturbations including stray fields and system defects. These make skyrmions very attractive for ultra-low power, high-density data storage and logic technologies. A key challenge to the development of skyrmion-based memory and logic devices is achieving skyrmion structures stable at ambient conditions (room temperature and no magnetic field).

Recently, we have realized ground-state magnetic skyrmions stable at ambient conditions by nanopatterning [1]. Specifically, cobalt nanodots with diameters of 560 nm and heights of 30 nm are patterned. The magnetic "vortex" configuration within these dots, shown in Fig. 1 (red), form a closed winding structure, with an out-of-plane core, which is stable over a wide range of temperatures. However, a vortex lacks an out-of-plane perimeter, distinguishing it from a skyrmion. By placing a vortex-state nanodot on top of a magnetic film, the loop structure and core can be imprinted into the film. Thus, by designing a film with an out-of-plane orientation, the imprinted structure at the interface has a closed loop structure with an out-of-plane core and perimeter, e.g. a skyrmion. To prove this claim and demonstrate its viability for application, three pieces of evidence must be shown: (1) the direction of circulation of the loop structure, called the circularity, must be controllable, (2) the orientation of the core, called the polarity, relative to the perimeter must be controllable, and (3) the loop structure must, in-fact, be imprinted into the film underlayer.

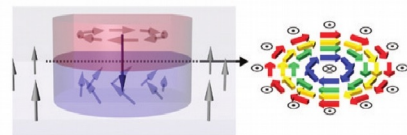


FIGURE 1: Diagram of an artificial skyrmion. Vortex dot is shown in red. The imprinted region (blue) that forms a skyrmion with the underlayer is shown in grey.

Samples were prepared by a three-step process. In step one, multilayer films of  $[\text{Co}(0.5 \text{ nm})/\text{Pd}(1 \text{ nm})]_{10}$  were grown on naturally oxidized Si substrates; the multilayer structure gives the film a preferred out-of-plane orientation - called the perpendicular magnetic anisotropy (PMA). In the second step, hexagonal arrays of nano-holes with a diameter of 560 nm and center-to-center spacing of 1000 nm were patterned into a  $\approx 400 \text{ nm}$  thick polymer layer that was spin-coated onto the Co/Pd film. The holes are shaped like a circle, with one side made flat; the asymmetric structure has been previously used to realize circularity control. Next, the sample was irradiated by 1 keV  $\text{Ar}^+$  plasma, which suppresses the PMA in the regions exposed by the holes, while the regions still protected by polymer retain their PMA. During the third step, 32 nm of Co was deposited into the holes and the polymer mask removed, realizing asymmetric Co dots grown over the irradiated regions. Once the sample was fabricated, the skyrmion state was configured by a designed field sequence. First, the Co/Pd underlayer was saturated in the positive out-of-plane direction using a large out-of-plane magnetic field. Then, the out-of-plane field was removed and a small in-plane magnetic field was applied to saturate the dots parallel to the flat edge. At this point a small out-of-plane magnetic field was applied anti-parallel to the underlayer. The in-plane magnetic field was removed, nucleating a vortex, with the core biased to be anti-parallel to the underlayer. Lastly, the out-of-plane magnetic field was removed, leaving the system at remanence (no magnetic field) in a vortex state dot, with a core anti-parallel to the underlayer, and the region under the dot having no PMA.

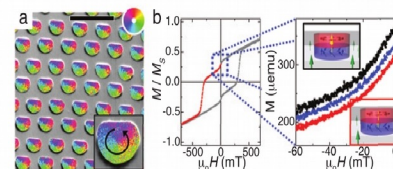


FIGURE 2: (a) SEMPA image of the asymmetric dot array. Color wheel indicates magnetization direction. (b) Remnant magnetization curve, with the core parallel, anti-parallel, and random relative to the underlayer, shown in black, red and blue, respectively ( $1 \mu = 10^{-3} \text{ A m}^2$ ).

As stated above, circularity control was achieved by using the asymmetric dot structure. Applying an in-plane magnetic field parallel to the flat edge of the dot defines the nucleation site for the vortex and thus the circularity. Micrographs taken using scanning electron microscopy with polarization analysis (SEMPA) are shown in Fig. 2(a). The colors indicate the direction of the magnetization; the common color wheel for each of the dots indicates a common circularity of the magnetization. Other magnetic imaging technique and magnetometry measurements confirm the circularity control seen in SEMPA.

Recalling the magnetic field sequence to set the skyrmion state, polarity control is determined during the vortex nucleation by the small magnetic field applied anti-parallel to the underlayer. To demonstrate polarity control, the remanent magnetization was measured with the core parallel and anti-parallel to the underlayer. Specifically, the sample was prepared as discussed above, with the core anti-parallel to the underlayer and the out-of-plane magnetization measured as the magnetic field was decreased from remanence to negative saturation. In this case the magnetization of the core and perimeter are opposite, and thus subtract when measured together. Then, the sample was prepared again, but with the biasing field applied parallel to the underlayer. In contrast to the former case, the magnetization from the core and underlayer are expected to be parallel and add together. In a third measurement no biasing field was applied and the polarity was random. Indeed, as shown in Fig. 2(b), the skyrmion state, with the core and underlayer anti-parallel, has the smallest magnetization; the vortex state with the core and the underlayer oriented parallel has the largest magnetization; the random polarity falls in-between the parallel and anti-parallel configurations. This confirms the biasing field indeed defines the polarity.

Lastly, and arguably most crucially, the imprinting of the skyrmion was demonstrated using polarized neutron reflectometry (PNR), performed on the MAGIK reflectometer. PNR is a technique that uses scattering to extract depth-profiles from layered systems and possesses sensitivity to nuclear and magnetic features. The measured data are shown as dots in Fig. 3(a). A model was made to simulate the nominal structure and the reflectivity pattern calculated. By iteratively changing the model and comparing the calculated reflectivity to the data, the model converges on an accurate representation of the physical system. The

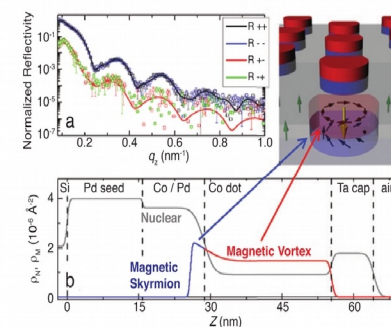


FIGURE 3: (a) Measured (dots) and simulated (lines) reflectometry, and (b) converged depth profile.

converged model is shown in Fig. 3(b), and the corresponding reflectometry is shown as the solid lines in Fig. 3(a), which agree well with the experimental data ( $\chi^2 < 1.2$ ). The converged model correctly identifies the designed structure, giving confidence in its accuracy. More importantly, the model identifies the magnetization of the Co dot - as expected - but also shows that the magnetization extends  $\approx 3 \text{ nm}$  below the [Co/Pd]/Co-dot interface. This imprinted magnetic feature is the first direct evidence of the imprinted magnetic skyrmion. Further, the imprinted skyrmion is expected to be stable while the dots and underlayer are stable (ambient conditions up-to approximately 300 °C, and 300 mT). Theoretical modeling using NIST's object oriented micromagnetic framework (OOMMF) confirms that the imprinted structure extends 2 nm into the underlayer.

In summary, we have successfully achieved room temperature artificial skyrmion lattices in the ground state over extended areas, defining a platform for exploring skyrmion properties and behaviors as well as the use of skyrmion lattices in novel technological concepts. The system is constructed by fabricating circularity controlled Co nanodots on a selectively irradiated Co/Pd underlayer with PMA. Circularity control is imposed by the fabrication of asymmetric dots and confirmed by microscopy. Polarity control is realized by the application of a small out-of-plane magnetic field during the vortex nucleation, and demonstrated in the magnetization curves. The imprinted skyrmion lattice in the Co/Pd is directly confirmed by PNR, and is quantitatively consistent with micromagnetic simulations. These artificially constructed skyrmion lattices are stable over a wide range of magnetic fields and temperatures, including room temperature and zero magnetic field. These foundational results present a new path in skyrmion research on the meso-scale, at and above room temperature.

## Reference

- [1] D. A. Gilbert, B. B. Maranville, A. L. Balk, B. J. Kirby, P. Fischer, D. T. Pierce, J. Unguris, J. A. Borchers, K. Liu, Nature Communications **6**, 8462 (2015).

<sup>1</sup> University of California, Davis, CA 95616

<sup>2</sup> NIST Center for Neutron Research, National Institute of Standards and Technology, Gaithersburg, MD 20899

<sup>3</sup> Center for Nanoscale Science and Technology, National Institute of Standards and Technology, Gaithersburg, MD 20899

<sup>4</sup> University of Maryland, College Park, MD 20742

<sup>5</sup> Lawrence Berkeley National Laboratory, Berkeley, CA 94720

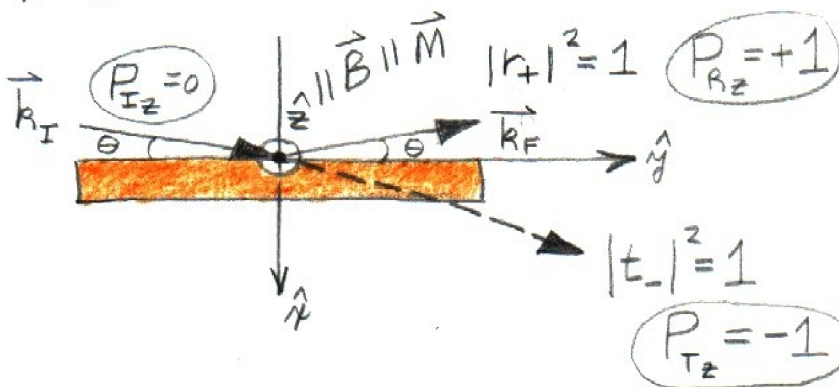
<sup>6</sup> University of California, Santa Cruz, CA 94056



# NEUTRON POLARIZER

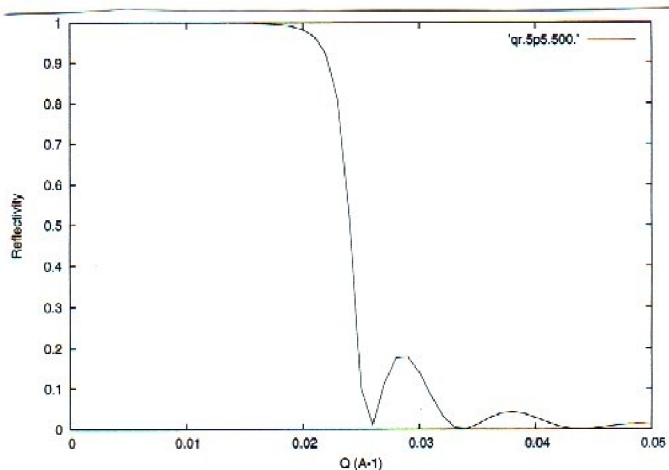
5C

By reflection from a magnetic film with nuclear and magnetic scattering length densities such that  $P_N - P_M = 0$  (for "-" spin state) and  $P_N + P_M \neq 0$  (for "+" spin state).



An unpolarized beam of neutrons can be polarized in a number of ways via interaction with a saturated ferromagnetic material. Perhaps the simplest involves specular reflection from a ferromagnetic plate with its magnetization saturated in the plane of the surface and normal to the wavevector transfer  $\mathbf{Q}$ , as depicted in the figure to the left. Note that by matching the nuclear and magnetic SLDs of the material, one spin state will see a net interaction potential which is zero whereas the other will experience a net positive value. Consequently, one spin state is transmitted and the other reflected, thereby separating + and - neutrons in space.

$$|r_+|^2 = 0, \quad |t_-|^2 = 1$$



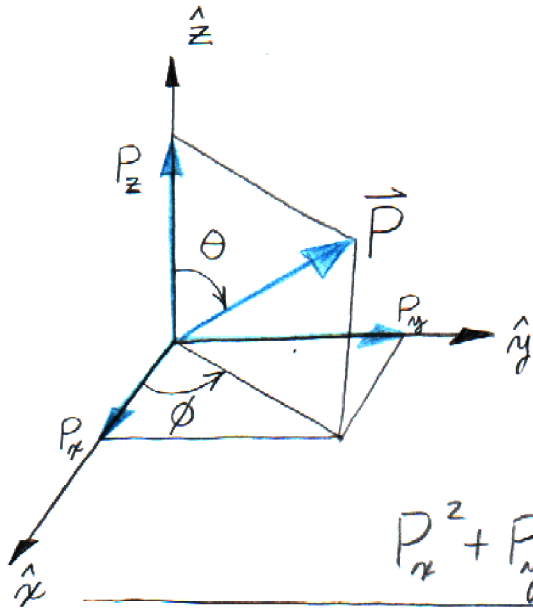
(CALCULATED USING FORMULAS OF FIGURE 3)

$$Q = 2k_{0x} = 2k_0 \sin \theta$$

$$P_N + P_M = 10.0 \times 10^{-6} \text{\AA}^{-2}$$

$$P_N - P_M = 0.0 \quad L = 500 \text{\AA}$$

# Neutron Polarization Vector



$P_x$	$P_y$	$P_z$	$\theta$	$\phi$	$C_+$	$C_-$
0	0	1	0	0	1	0
0	0	-1	$\pi$	0	0	1
1	0	0	$\pi/2$	0	$1/\sqrt{2}$	$1/\sqrt{2}$
0	1	0	$\pi/2$	$\pi/2$	$1/\sqrt{2}$	$i/\sqrt{2}$

$$\vec{P} = P_x \hat{x} + P_y \hat{y} + P_z \hat{z}$$

$$P_x^2 + P_y^2 + P_z^2 = 1$$

$$P_x = \sin \theta \cos \phi = 2 \operatorname{Re}(C_+^* C_-)$$

$$P_y = \sin \theta \sin \phi = 2 \operatorname{Im}(C_+^* C_-)$$

$$P_z = \cos \theta = |C_+|^2 - |C_-|^2$$

$$P_z = \frac{N_+ - N_-}{N_+ + N_-} \quad |C_+|^2 = \frac{N_+}{N_+ + N_-} \quad |C_-|^2 = \frac{N_-}{N_+ + N_-}$$

$$|C_+|^2 + |C_-|^2 = 1$$

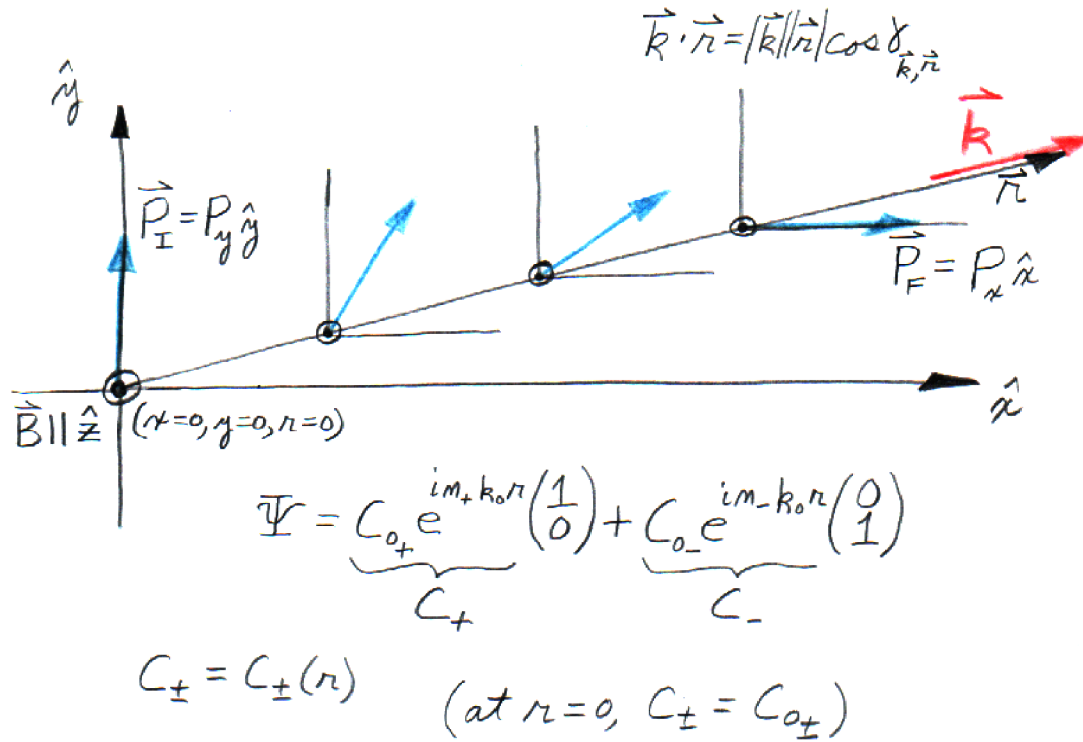
$$C_+ = \cos\left(\frac{\theta}{2}\right)$$

$$C_- = \sin\left(\frac{\theta}{2}\right) e^{i\phi}$$

It is possible to mathematically construct a "polarization" vector  $\mathbf{P}$  which describes some of the spin-dependent characteristics of an ensemble or collection of spin half neutrons composing a beam. The number of neutrons in the spin "+" or "-" eigenstates is  $N_+$  or  $N_-$ , respectively. The coefficients  $C_+$  and  $C_-$  of the spinor wave function for the neutron can be written in terms of these numbers and also can be related to the components of the polarization vector along the x-, y-, and z-directions.  $\mathbf{P}$  can alternatively be described in terms of angles relative to the coordinate axes.



# Polarization Rotation



A net magnetic induction  $\mathbf{B}$  defines an axis of quantization (conventionally taken to be parallel to the z-axis of a rectangular coordinate system or reference frame). Any component of the neutron polarization vector perpendicular to this  $\mathbf{B}$  field will rotate with a characteristic "Larmor" frequency that is proportional to the difference between spin + and - refractive indices.

e.g.:

$$\begin{aligned}
 P_y(r) &= 2 \operatorname{Im}(C_+^* C_-) \\
 &= 2 \operatorname{Im} \left[ C_+^* e^{-im_+ k_0 r} C_- e^{im_- k_0 r} \right] \\
 &= 2 \operatorname{Im} \left[ \left( \frac{1}{\sqrt{2}} \right) \left( \frac{i}{\sqrt{2}} \right) e^{i(m_- - m_+) k_0 r} \right] \\
 &= \operatorname{Im} \left[ i \cos((m_- - m_+) k_0 r) - \sin((m_- - m_+) k_0 r) \right] \\
 \boxed{P_y(r) = \cos[(m_- - m_+) k_0 r]} & \quad (P_y(r=0) = 1)
 \end{aligned}$$

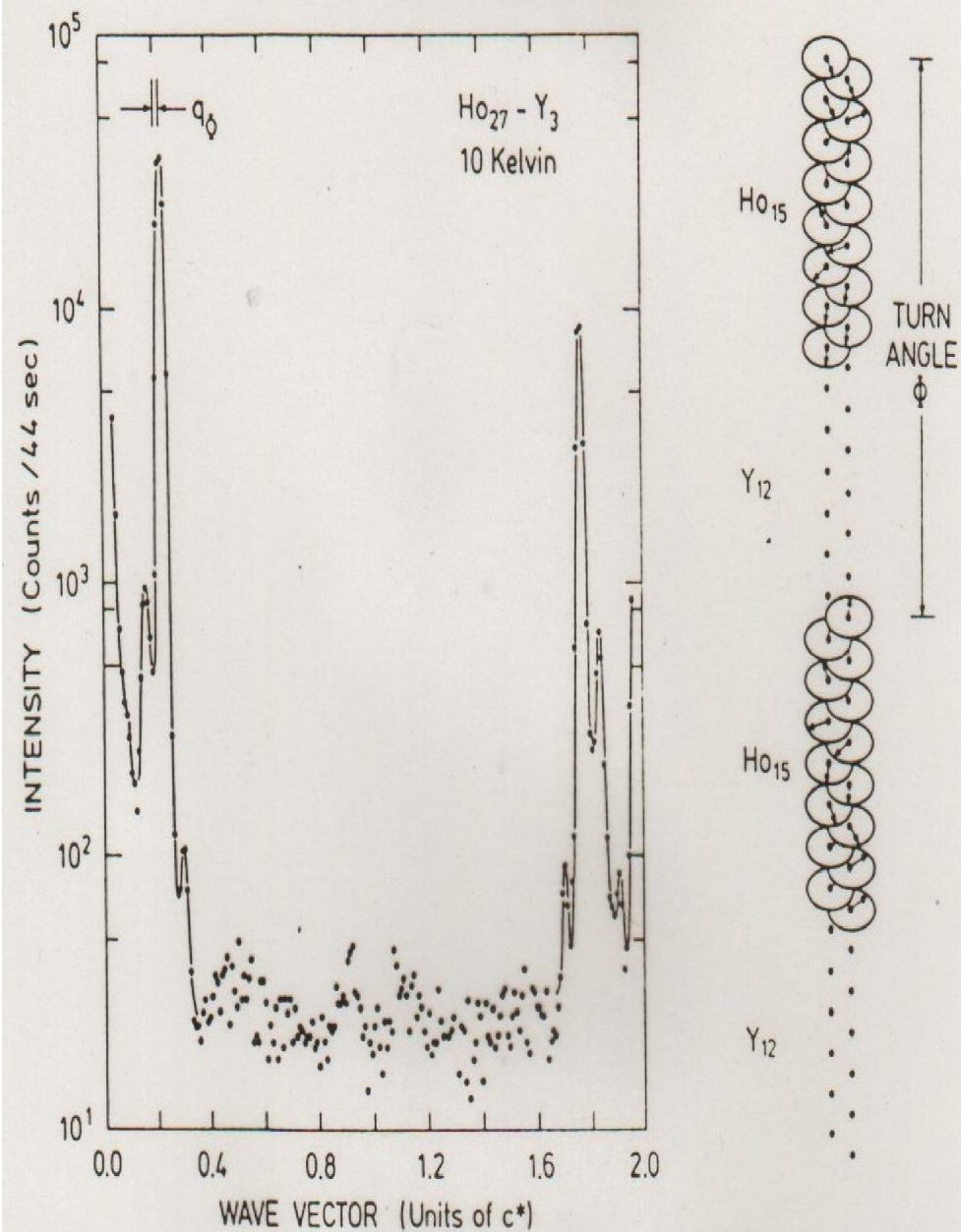


Figure 48. Neutron diffraction pattern obtained from the  $\text{Ho}_{27}\text{-Y}_3$  superlattice at 10 K. The features of the diffraction pattern are as in figure 8 showing long-range magnetic order. On the right of the figure is shown a schematic drawing of a superlattice explaining the phase advance  $\Phi$ . The data were taken at Brookhaven on the H9 instrument at the cold source at the HFBR. (After Bohr *et al.* 1989.)

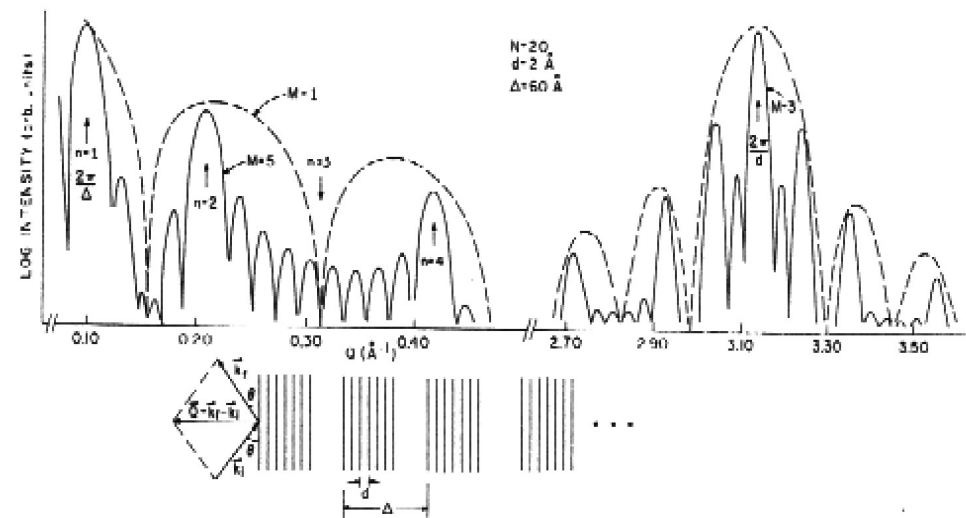
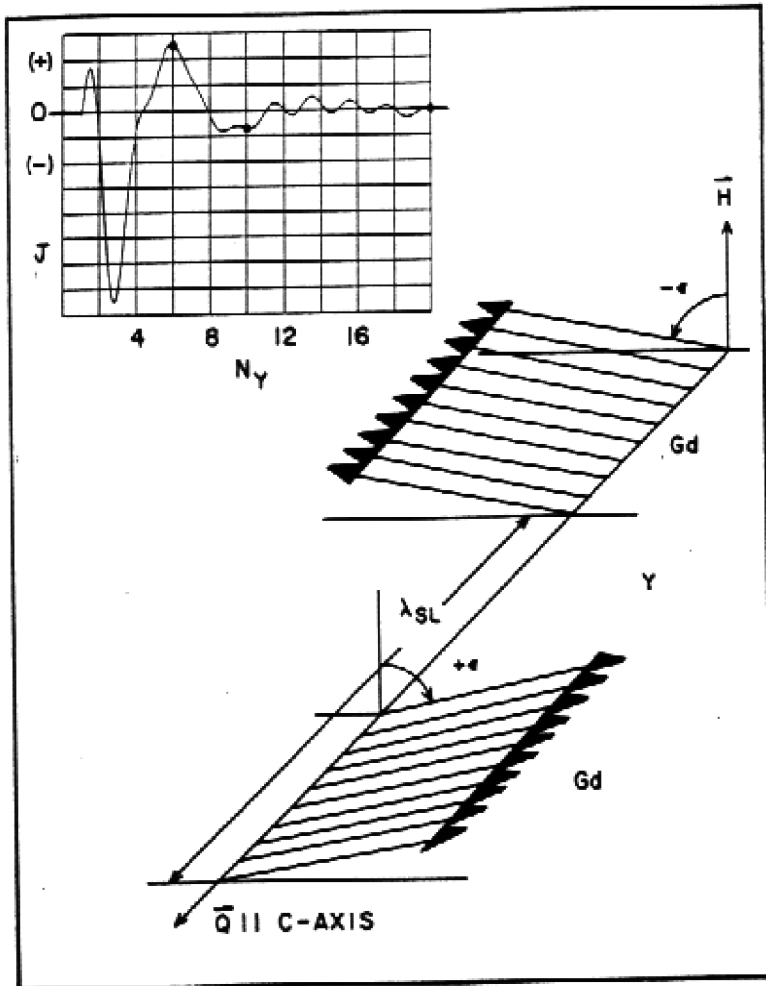


Figure 6. Diffraction pattern at low and high  $Q$  for an idealized superlattice consisting of  $M$  sets of  $N$  atomic planes with periodicities  $\Delta$  and  $d$ , as shown schematically in the lower part of the figure. Details are described in the text. (After Majkrzak 1986.)

$$\begin{aligned}
 R &= \left( \frac{4\pi}{Q} \right)^2 \left| \sum_{m=1}^M \sum_{n=1}^N \rho \exp(iQ(nd + m\Delta)) \right|^2 \\
 &= \left( \frac{4\pi}{Q} \right)^2 \rho^2 \left| \sum_{n=1}^N \exp(iQnd) \right|^2 \left| \sum_{m=1}^M \exp(iQm\Delta) \right|^2 \\
 &= \left( \frac{4\pi}{Q} \right)^2 \rho^2 \left| \frac{\sin(NQd/2)}{\sin(Qd/2)} \right|^2 \left| \frac{\sin(MQ\Delta/2)}{\sin(Q\Delta/2)} \right|^2
 \end{aligned}$$

That the spin structures of Gd-Y superlattices are dependent on the thickness (or number of atomic planes) of the intervening nonmagnetic Y layers arises because the Y serves as a medium through which successive ferromagnetic Gd layers are coupled by the Ruderman-Kittel-Kasuya-Yosida exchange interaction (mediated by conduction electrons) which is both long-range and oscillatory. The Y blocks, although they do not possess any localized magnetic moment, are conducting, thereby allowing the propagation of the interaction.



### **OBSERVATION OF A MAGNETIC ANTIPHASE DOMAIN-STRUCTURE WITH LONG-RANGE ORDER IN A SYNTHETIC GD-Y SUPERLATTICE**

MAJKRZAK, CF; CABLE, JW; KWO, J; HONG, M; MCWHAN, DB; YAFET, Y; WASZCZAK, JV; VETTIER, C  
 PHYSICAL REVIEW LETTERS Volume: 56 Issue: 25  
 Pages: 2700-2703 Published: JUN 23 1986

### **POLARIZED NEUTRON-DIFFRACTION STUDIES OF GD-Y SYNTHETIC SUPERLATTICES**

MAJKRZAK, CF; CABLE, JW; KWO, J; HONG, M; MCWHAN, DB; YAFET, Y; WASZCZAK, JV; GRIMM, H; VETTIER, C  
 JOURNAL OF APPLIED PHYSICS Volume: 61 Issue: 8  
 Pages: 4055-4057 Published: APR 15 1987

Approximately two years later, in 1988, Peter Gruenberg discovered the giant magneto-resistance effect in Fe/Cr multilayers. Afterwards, at NIST, neutron scattering studies of FeCr superlattices with John Ankner, Andreas Schreyer, Hartmut Zabel, and company, in collaboration with Peter Gruenberg and his group, revealed further details about the interlayer exchange coupling mechanism at work in the Fe/Cr system.

**DIRECT OBSERVATION OF NONCOLLINEAR SPIN STRUCTURES IN FE/CR(100) SUPERLATTICES USING SPIN-POLARIZED NEUTRON REFLECTIVITY**

SCHREYER, A; ANKNER, JF; ZABEL, H; SCHAFER, M; MAJKRZAK, CF; GRUNBERG, P  
PHYSICA B-CONDENSED MATTER Volume: 198 Issue: 1-3 Pages: 173-176 Pub: APR 1994

**DIRECT OBSERVATION OF A NONCOLLINEAR 50-DEGREES- COUPLED MAGNETIZATION PROFILE IN A FE/CR(001) SUPERLATTICE**

SCHREYER, A; ANKNER, JF; SCHAFER, M; ZEIDLER, T; ZABEL, H; MAJKRZAK, CF; GRUNBERG, P  
JOURNAL OF MAGNETISM AND MAGNETIC MATERIALS Volume: 148 Issue: 1-2 Pages: 189-190  
Published: JUL 1995

**Noncollinear and collinear magnetic structures in exchange coupled Fe/Cr(001) superlattices**

Schreyer, A; Ankner, JF; Zeidler, T; Zabel, H; Schafer, M; Wolf, JA; Grunberg, P; Majkrzak, CF  
PHYSICAL REVIEW B Volume: 52 Issue: 22 Pages: 16066-16085 Published: DEC 1 1995

# The Nobel Prize in Physics 2007

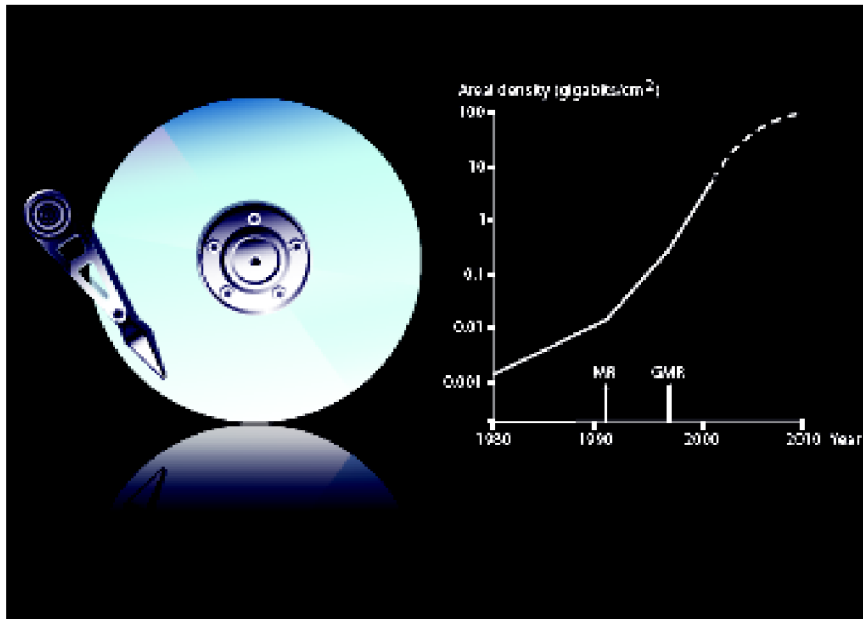
9 October 2007



*This year's Nobel Prize in Physics is awarded to ALBERT FERT and PETER GRÜNBERG for their discovery of Giant Magnetoresistance. Applications of this phenomenon have revolutionized techniques for retrieving data from hard disks. The discovery also plays a major role in various magnetic sensors as well as for the development of a new generation of electronics. The use of Giant Magnetoresistance can be regarded as one of the first major applications of nanotechnology.*

## Better read-out heads for pocket-size devices

Constantly diminishing electronics have become a matter of course in today's IT-world. The yearly addition to the market of ever more powerful and lighter computers is something we have all started to take for granted. In particular, hard disks have shrunk – the bulky box under your desk will soon be history when the same amount of data can just as easily be stored in a slender laptop. And with a music player in the pocket of each and everyone, few still stop to think about how many cds' worth of music its tiny hard disk can actually hold. Recently, the maximum storage capacity of hard disks for home use has soared to a terabyte (a thousand billion bytes).



Diagrams showing the accelerating pace of miniaturization might give a false impression of simplicity – as if this development followed a law of nature. In actual fact, the ongoing IT-revolution depends on an intricate interplay between fundamental scientific progress and technical fine tuning. This is just what the Nobel Prize in Physics for the year 2007 is about.

Scientific Background on the Nobel Prize in Physics 2007

## The Discovery of Giant Magnetoresistance

compiled by the Class for Physics of the Royal Swedish Academy of Sciences

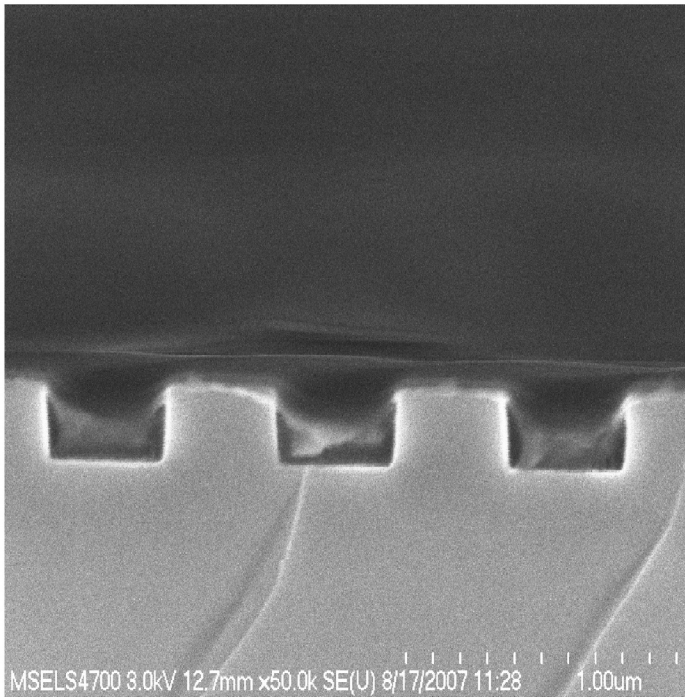
As recounted in the “Scientific Background” material referred to on the left side of the page, prior to the discovery of the GMR effect by Gruenberg, polarized neutron diffraction studies of magnetic superlattices revealed an unambiguous coupling between magnetic layers across intervening nonmagnetic spacers. The interlayer coupling (IEC) observed in this neutron diffraction work was explained in terms of long-range exchange interactions, for example, the RKKY (Ruderman Kittel Kasuya Yosida) interaction. Interestingly, the underlying mechanism responsible for GMR was thus known about before the effect itself was discovered!

# Off-Specular Neutron Reflection

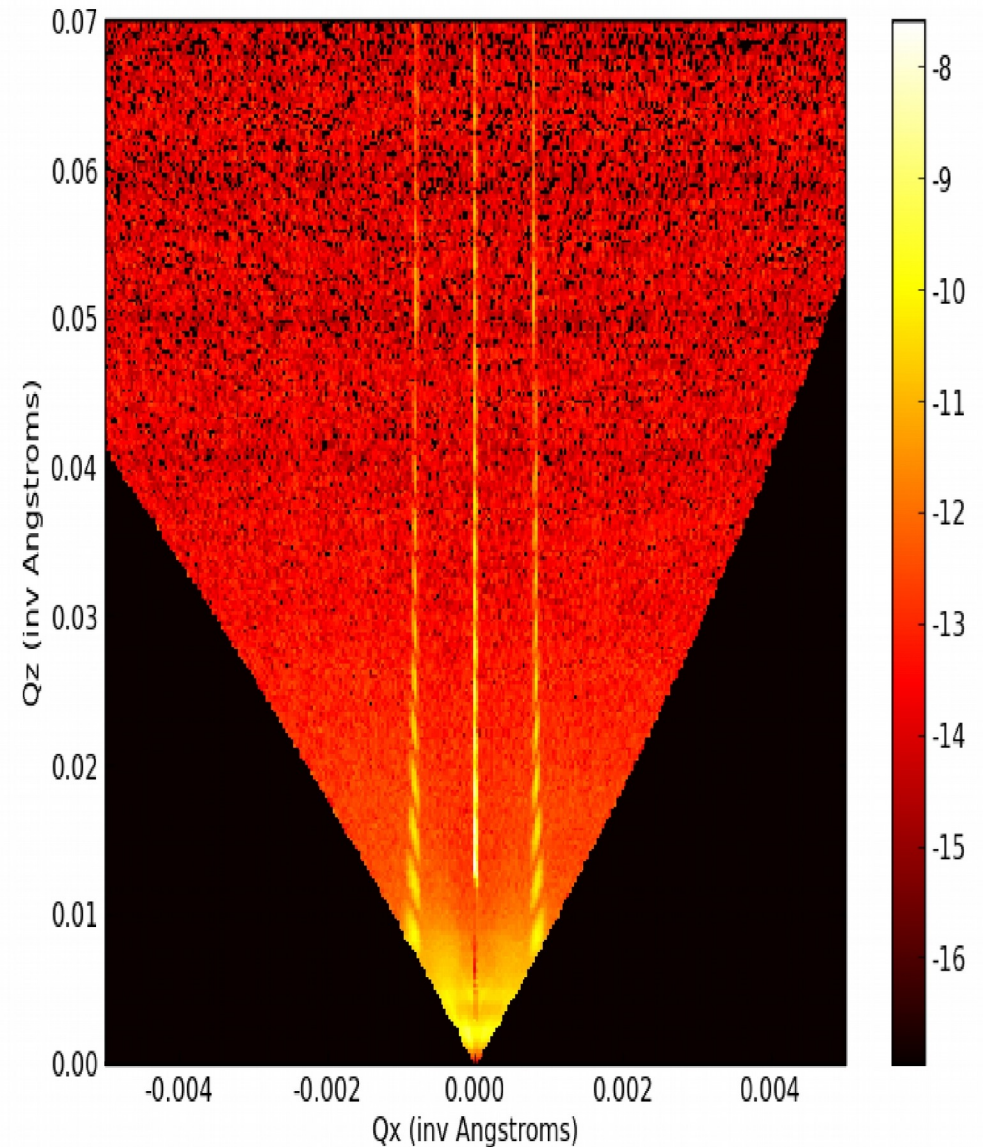


## Diblock copolymer lamellar nanostructures –

R.Jones, B.Berry, and K.Yager (NIST Polymer Division) and  
S.Satija, J.Dura, B.Maranville et al. (NCNR).



Side-view scanning-electron micrograph of laser-interferometry-produced silicon substrate with 400 nm channels, spaced by 400 nm for a total repeat distance of 800 nm.



Neutron diffraction from silicon with channels cut in the surface in a periodic grating structure (as shown in the previous slide) without any material in the troughs. Using a position-sensitive-detector, both specular reflectivity (along the vertical  $Q_z$  axis) and non-specular (along the horizontal  $Q_x$  axis) can be collected.



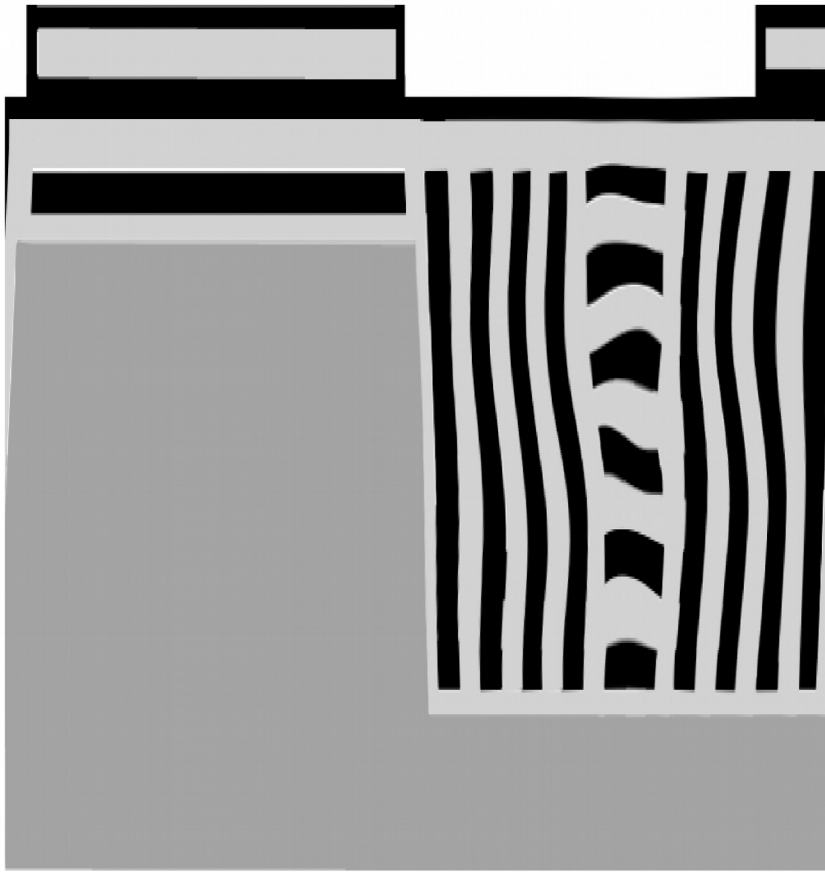
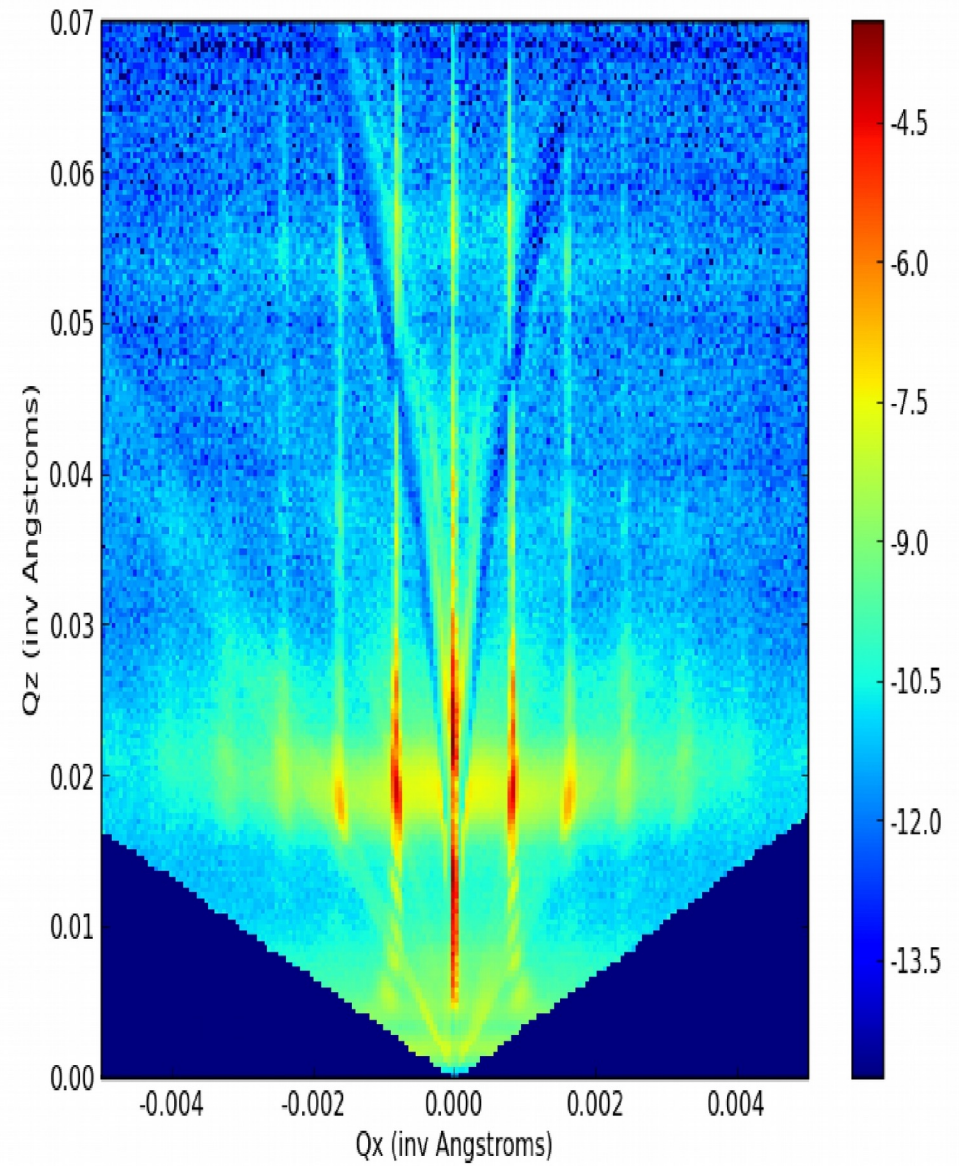


Diagram of expected orientation of di-block copolymer lamellae, with respect to the channels in the Si. The silicon substrate with etched channels is displayed in gray, with other lighter and darker regions corresponding to the two separate polymer components of the lamellae.



Neutron diffraction from Si channels filled with ordered di-block copolymer.



# On-Line Analysis of Neutron Reflectivity Data

# Interactive, Web-Based Calculator of Neutron and X-ray Reflectivity

Brian B. Maranville

National Institute of Standards and Technology,  
Gaithersburg, MD 20899, USA

[brian.maranville@nist.gov](mailto:brian.maranville@nist.gov)

Software DOI: <https://doi.org/10.18434/M3QG67>

Software Version: 1.0

Key words: calculator; neutron; reflectivity; scattering.

Accepted: June 30, 2017

Published: July 12, 2017

<https://doi.org/10.6028/jres.122.034>

## 1. Summary

For many users of the neutron and X-ray reflectometry instruments at NIST, these measurements represent a relatively small and specialized part of their research portfolio. As such, providing calculation and modeling tools that are as accessible and easy-to-use as possible is a high priority of the facility. In order to meet this need, a purely web-browser-based calculator for reflectivity modeling and rudimentary fitting has been developed and provided on a publicly accessible web server.

Going to <https://www.ncnr.nist.gov/instruments/magik/calculators/reflectivity-calculator.html>, will load a one-page web application into the browser. Any relatively modern browser with support for ECMAScript 5 will be able to load and run the application. A calculator for magnetic samples can be found at <https://www.ncnr.nist.gov/instruments/magik/calculators/magnetic-reflectivity-calculator.html>.

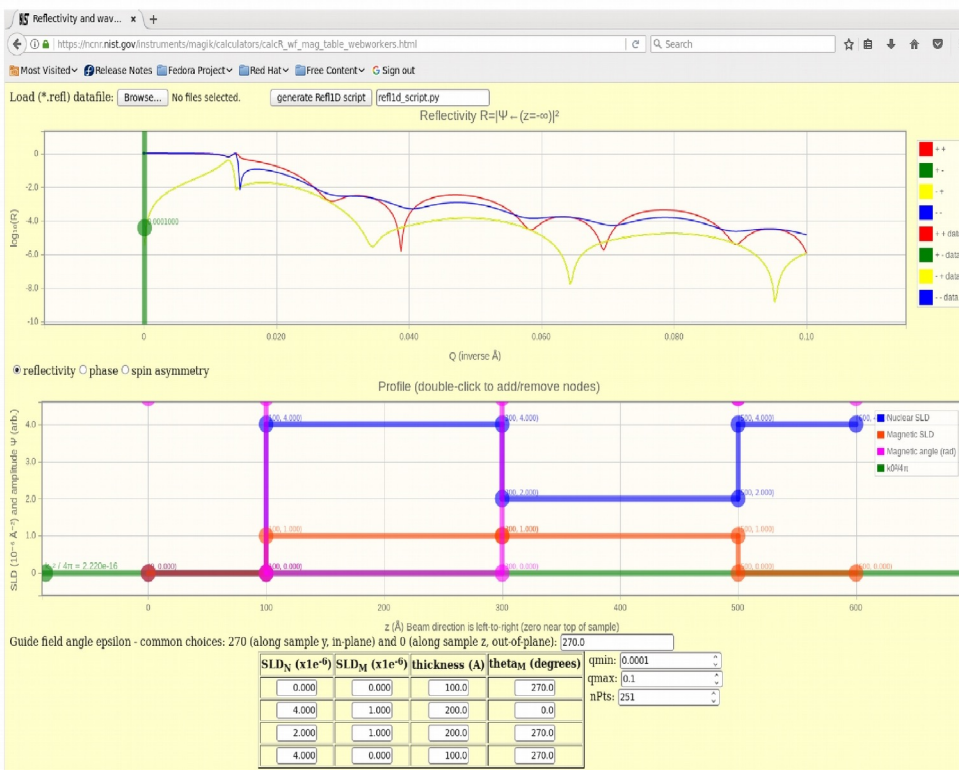
**Neutron activation and scattering calculator**

This calculator uses neutron cross sections to compute activation on the sample given the mass in the sample and the time in the beam, or to perform scattering calculations for the neutrons which are not absorbed by the sample.

1. Enter the sample formula in the material panel.
2. To perform activation calculations, fill in the thermal flux, the mass, the time on and off the beam, then press the calculate button in the neutron activation panel.
3. To perform scattering calculations, fill in the wavelength of the neutron and/or x-rays, the thickness and the density (if not given in the formula), then press the calculate button in the absorption and scattering panel.

Questions?  
Neutron activation: Dave Brown <[david.brown@nist.gov](mailto:david.brown@nist.gov)>  
Scattering calculations: Paul Kienzle <[paul.kienzle@nist.gov](mailto:paul.kienzle@nist.gov)>

Last modified 11-May-2017 by website owner: NCNR (attn: Paul Kienzle)



On-line programs for calculating scattering length densities and specular neutron reflectivity – fitting programs are also available. (Developed and maintained by NCNR staff, particularly Brian Maranville and Paul Kienzle.)

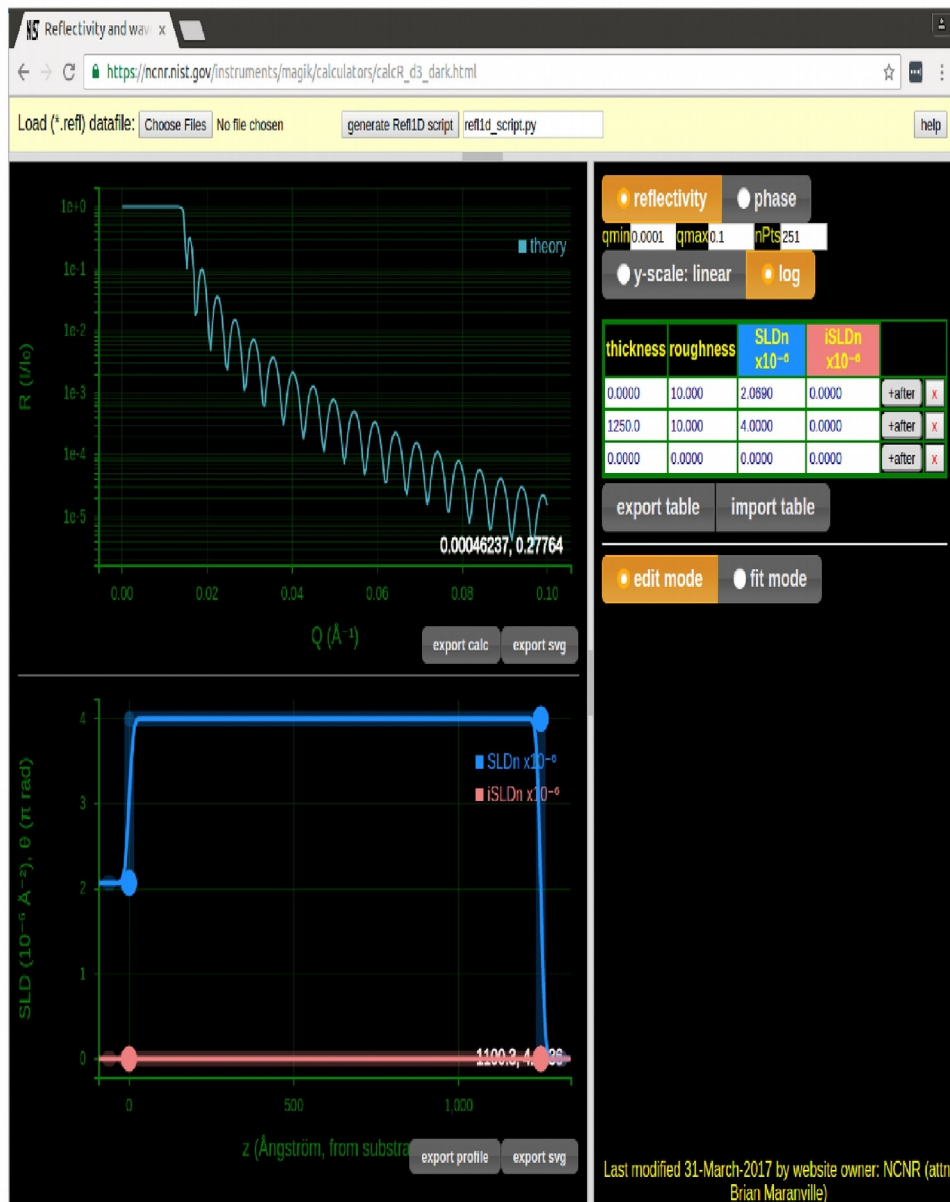


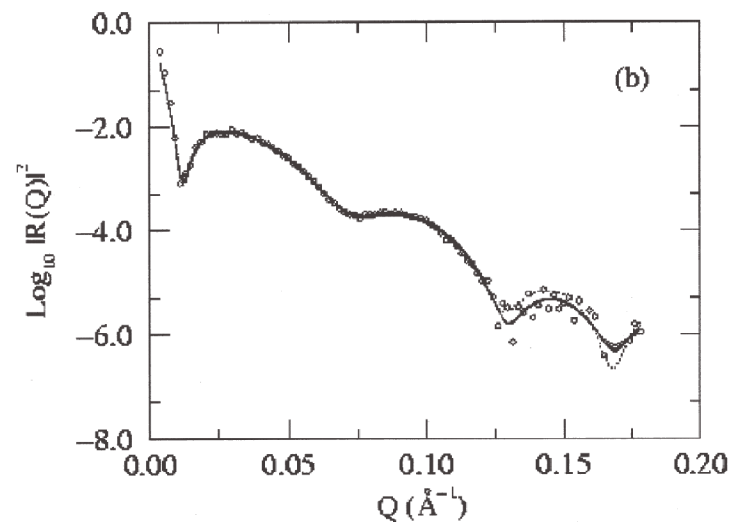
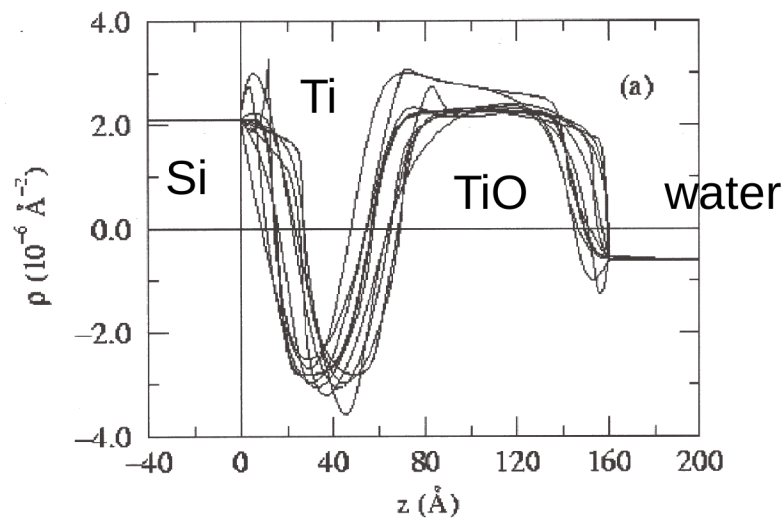
Fig. 1. Screenshot of non-magnetic reflectivity calculator.



Fig. 2. Screenshot of magnetic reflectivity calculator.

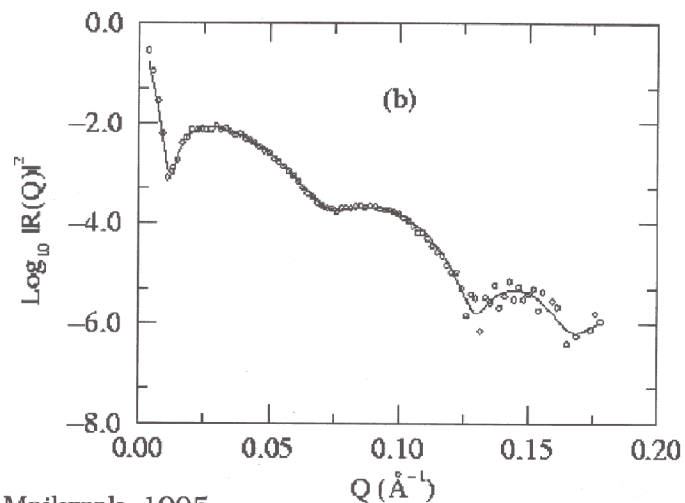
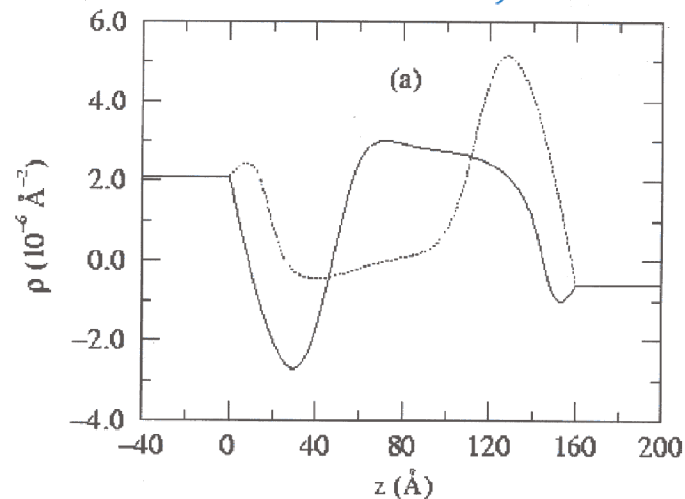
# Phase-Sensitive Neutron Reflectometry

# A specific illustration of the phase problem in specular neutron reflectometry:



Repeated fits of reflectivity data from a Ti/TiO film system on a Si substrate in contact with an aqueous reservoir (Berk et al.). The variation among the individual fits is indicative of the accuracy attainable in the SLD profile given the truncation of the reflectivity data at a maximum value of Q and the statistical uncertainty in the data points.

## TiO in situ: Wiesler, et al.

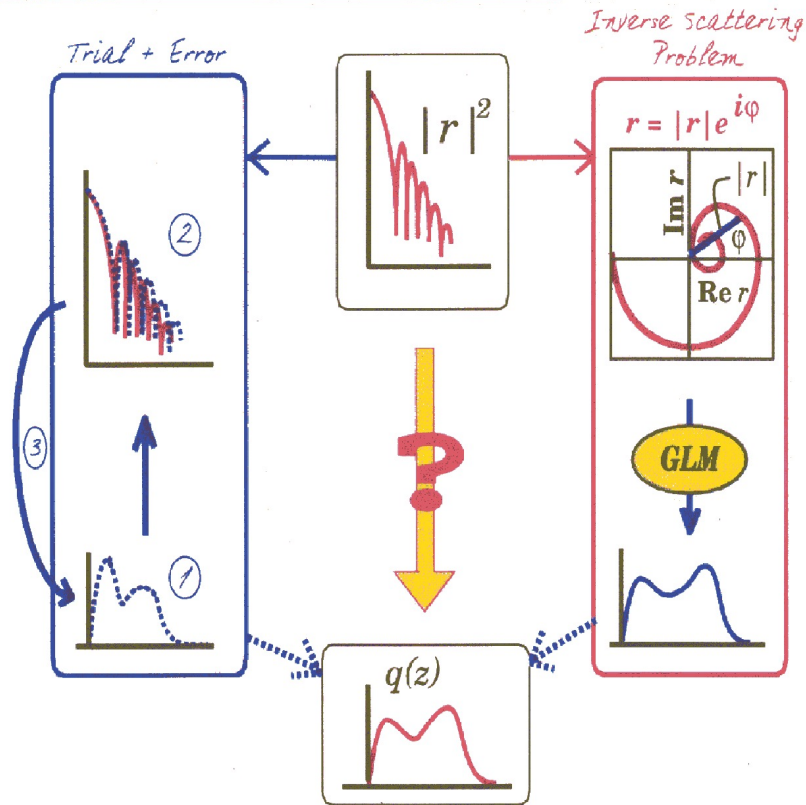


Berk & Majkrzak, 1995

It was found that if enough individual fits were performed, another “family” of fits emerged (only one of which is shown above in comparison to a representative fit of the other family shown on the previous slide) with essentially the same chi-squared goodness of fit criteria -- this alternative SLD profile is a consequence of the loss of phase information inherent when the reflectivity  $|r|^2$  (proportional to the reflected intensity) is measured rather than the complex reflection amplitude  $r$  -- i.e., the non uniqueness arises from a loss of the phase information carried by the reflected wave function.



# Inverting reflectivity



(after N.F. Berk)

Theoretically, Norm and several others, including Paul Sacks, Lipperheide, and Leeb, realized, that the one-dimensional specular reflectivity could be directly inverted **if** the reflected wave *amplitude* and not just the intensity as measured was known.

FOURIER TRANSFORM  
OF THE COMPLEX  
REFLECTION  
AMPLITUDE

$$\mathcal{R}(z) = \frac{1}{\pi} \operatorname{Re} \int_0^{\infty} r(k_z) e^{ik_z z} dk_z$$

GELFAND  
LEVITAN  
MARCHENKO  
INTEGRAL  
EQUATION

$$K(z, \gamma) + \mathcal{R}(z+\gamma) + \int_{-z}^{+z} K(z, x) \mathcal{R}(x+\gamma) dx = 0$$

SCATTERING  
LENGTH  
DENSITY

$$\rho(z) = 2 \frac{dK(z, z)}{dz}$$

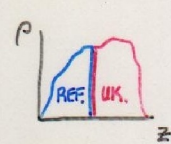
GIVEN THE COMPLEX REFLECTION AMPLITUDE, THE SCATTERING LENGTH DENSITY  $\rho$  CAN BE OBTAINED FROM AN EXACT, FIRST PRINCIPLE INVERSION FOR A REAL POTENTIAL OF FINITE EXTENT — AND THE SOLUTION IS UNIQUE!

NO FITTING, NO ADJUSTABLE PARAMETERS



But how do you determine the reflection amplitude as a function of  $Q$  from measured reflected intensity? Thinking about the piece-wise continuous solution method of the Shroedinger wave equation provided the answer . . .

FORMALISM ALLOWS A COMPOSITE POTENTIAL TO BE EXPRESSED AS A PRODUCT:

$$\begin{pmatrix} A & B \\ C & D \end{pmatrix} = \begin{pmatrix} a & b \\ c & d \end{pmatrix} \begin{pmatrix} w & x \\ y & z \end{pmatrix}$$


COMPOSITE (1,2,3)      UNKNOWN      REFERENCE (1,2,3)

$$|R(Q)|^2 = |R_1(Q)|^2, |R_2(Q)|^2, \text{ and } |R_3(Q)|^2$$

$$\Sigma_i \equiv 2 \left[ \frac{1 + |R_i|^2}{1 - |R_i|^2} \right] = A_i^2 + B_i^2 + C_i^2 + D_i^2$$

$$A_i^2 = a^2 w_i^2 + b^2 y_i^2 + 2abw_i y_i$$

$$C_i^2 = c^2 w_i^2 + d^2 y_i^2 + 2cdw_i y_i$$

$$B_i^2 = a^2 x_i^2 + b^2 z_i^2 + 2abx_i z_i$$

$$D_i^2 = c^2 x_i^2 + d^2 z_i^2 + 2cdx_i z_i$$

(INDEPENDENTLY AT EACH  $Q$ )

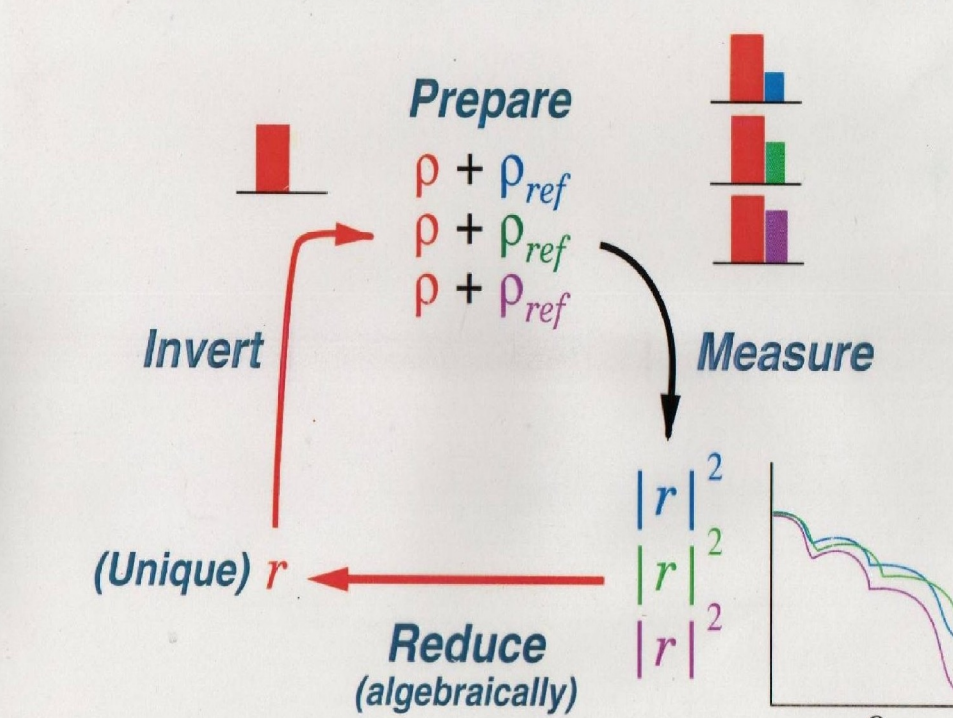
$$\Sigma_i = \underbrace{(w_i^2 + x_i^2)}_{\text{REF}} \alpha + \underbrace{(y_i^2 + z_i^2)}_{\text{REF}} \beta + 2(w_i y_i + x_i z_i) \gamma$$

$\alpha = a^2 + c^2$   
 $\beta = b^2 + d^2$   
 $\gamma = ab + cd$

$i = 1, 2, 3$       SOLVE FOR UNKNOWN  $\alpha, \beta,$  AND  $\gamma$  TO GET

$$R_{\text{UNKNOWN}} = \frac{(\beta - \alpha) - 2i\gamma}{2 + \beta + \alpha}$$

### Phase Determination with 3 References




Prepare  
 $\rho + \rho_{ref}$   
 $\rho + \rho_{ref}$   
 $\rho + \rho_{ref}$

Measure

Reduce (algebraically)

(Unique)  $r$

Invert



Majkrzak & Berk, 1995  
 de Haan, et al., 1995

### Phase determination

C.F. Majkrzak and N.F. Berk, Phys. Rev. B **52**, 10827 (1995).  
 V.-O. de Haan, et al., Phys. Rev. B **52**, 10830 (1995).